RESEARCH ARTICLE SUMMARY

METALLURGY

Extra strengthening and work hardening in gradient nanotwinned metals

Zhao Cheng*, Haofei Zhou*, Qiuhong Lu, Huajian Gao†, Lei Lu†

INTRODUCTION: Gradient structures ubiquitously exist in natural materials such as bone, shells, and trees. Microstructural gradients are increasingly being introduced into a wide range of engineering materials, providing them with enhanced strength, hardness, work hardening, ductility, and fatigue resistance through deformation mechanisms that are distinct from those operating in gradient-free counterparts. However, understanding structural gradient–related mechanical behaviors in all gradient structures, including those in engineering materials, has been challenging.

Although control of the structural gradient is essential to achieving optimized mechanical behaviors, existing manufacturing approaches are limiting for bulk gradient materials. For instance, surface tooling and mechanical treatments generate either limited volume fractions of gradient layers localized only near the surface or a negligible degree of structural gradient along the gradient direction. All of these limit our ability to tailor the mechanical properties and understand the deformation mechanisms of gradient-structured metals.

RATIONALE: We used a direct-current electrodeposition method to synthesize bulk gradient nanotwinned pure Cu samples with controllable patterning of homogeneous nanotwinned components. The individual components are composed of high-density, preferentially oriented nanometer-scale twin boundaries embedded within micrometer-scale columnar-shaped grains. We observed gradient-induced enhancements in both tensile strength and work-hardening rate through a wide range of structural gradients (in both twin boundary spacing and grain size) that span across the entire thickness of the sample. We combined scanning electron microscopy, a two-beam diffraction technique in transmission electron microscopy, and massively parallel atomistic simulations to identify the underlying strengthening mechanism in gradient nanotwinned Cu. We also prepared homogeneous nanotwinned samples as controls to demonstrate the importance of the structural gradient.

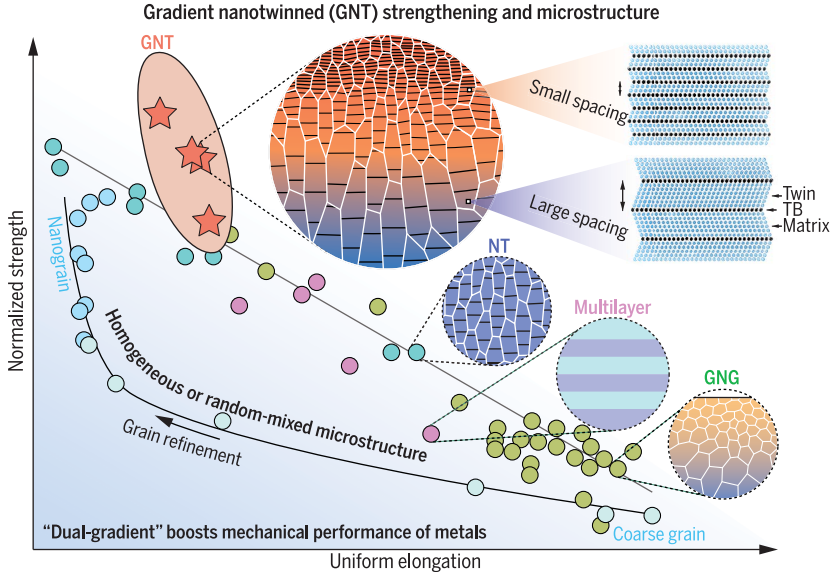

Highly tunable structural gradient for extra strengthening and ductility in metals. A gradient nanotwinned microstructure with a spatial gradient in both twin boundary (TB) spacing and grain size offers an unusual combination of strength, uniform elongation, and work hardening, which is superior to its strongest component and to existing heterogeneous strengthening approaches through gradient nanograined (GNG), homogeneous nanotwinned (NT), and multilayered microstructures.

RESULTS: Our findings indicate that simultaneous enhancement in strength and work hardening can be achieved by solely increasing the structural gradient in pure Cu. The maximum structural gradient led to an improved work-hardening rate and tensile strength that can exceed even the strongest component of the gradient microstructure—an unusual phenomenon that appears to be absent from the existing literature on metals and alloys with gradient nanograined or any other heterogeneous microstructures. We attribute the extra strengthening and work hardening of gradient nanotwinned structures to the unique patterning of geometrically necessary dislocations in the form of bundles of concentrated dislocations uniformly distributed in grain interiors. Such dislocation patterns in grain interiors are fundamentally different from randomly distributed, statistically stored dislocations in homogeneous structures. The bundles of concentrated dislocations with ultrahigh density of dislocations act as strong obstacles to slip, help to delocalize plastic deformation inside the grains, and accelerate the work-hardening process.

ON OUR WEBSITE

Read the full article at http://dx.doi.org/10.1126/science.aau1925

CONCLUSION: In our simple bottom-up approach to create gradient nanotwinned structure in pure Cu, a large structural gradient allows for an exceptional combination of high strength and work hardening that can exceed even the strongest component of the gradient structure. Both experimental and computational evidence suggest the importance of covering the whole structure with tunable structural gradients for the development of high densities of dislocations in grain interiors. The gradient nanotwinned strengthening concept proposed in this work provides insights into combining structural gradients at different length scales in order to push forward the strength limit of materials and may be essential to creating the next generation of metals with both high strength and high ductility. ■

The list of author affiliations is available in the full article online.
*These authors contributed equally to this work.
†Corresponding author. Email: huajian_gao@brown.edu (H.G.); llu@imr.ac.cn (L.L.)
Cite this article as Z. Cheng *et al.*, *Science* **362**, eaau1925 (2018). DOI: 10.1126/science.aau1925

RESEARCH ARTICLE

METALLURGY

Extra strengthening and work hardening in gradient nanotwinned metals

Zhao Cheng[1,2]*, Haofei Zhou[3]*, Qiuhong Lu[1], Huajian Gao[3]†, Lei Lu[1]†

Gradient structures exist ubiquitously in nature and are increasingly being introduced in engineering. However, understanding structural gradient–related mechanical behaviors in all gradient structures, including those in engineering materials, has been challenging. We explored the mechanical performance of a gradient nanotwinned structure with highly tunable structural gradients in pure copper. A large structural gradient allows for superior work hardening and strength that can exceed those of the strongest component of the gradient structure. We found through systematic experiments and atomistic simulations that this unusual behavior is afforded by a unique patterning of ultrahigh densities of dislocations in the grain interiors. These observations not only shed light on gradient structures, but may also indicate a promising route for improving the mechanical properties of materials through gradient design.

Making metals stronger and tougher by tailoring their microstructures has been an enduring pursuit in materials science and engineering (*1*–*3*). Gradient metals have emerged as a class of hierarchical materials with tunable distribution of microstructures (*4*–*8*). As a result of the substantial strain gradients (*9*–*13*) intrinsic to these materials, gradient metals could be designed to exhibit an unusual combination of high strength and hardness, considerable ductility, and enhanced strain hardening and fatigue resistance (*4*–*6*, *14*). However, it remains a challenge to understand the underlying mechanisms that control the strengthening of gradient materials because of the often complex dislocation structures in plastic deformation (*6*, *15*, *16*).

Meanwhile, the design of nanotwinned structures has been recognized as a universal strategy in the pursuit of superior mechanical and physical properties (*1*, *5*, *17*–*20*). Various processing techniques have been adopted to synthesize highly oriented nanotwinned structures (*20*) in a range of pure metals and alloys (*21*). Such materials usually exhibit plastic anisotropy, as their deformation mechanisms are strongly dependent on the orientation of loading axis with respect to the twin boundaries (TBs) (*18*, *22*, *23*). When the loading direction is oriented in parallel to the twin planes, single slip by threading dislocations (*18*) is activated—a mechanism similar to one previously observed in thin films and nanolaminated metallic composites (*24*, *25*). Most recently, a history-independent and stable cyclic response in highly oriented nanotwinned copper was reported (*19*). Such unique cyclic behavior is governed by a type of correlated "necklace" dislocations formed by the linking of threading dislocations in adjacent twins, leading to a superstable twin structure and negligible cyclic damage, which is fundamentally distinct from the inevitably irreversible damage accumulation in single-crystal, coarse-grained, ultrafine-grained, and nanograined metals (*19*).

We performed experiments and atomistic simulations on bulk copper samples with a controllable spatial gradient in the highly oriented nanotwinned structure. We found an interesting strengthening effect and obtained simultaneous enhancement in strength and work hardening by increasing the structure gradient. By taking advantage of the simple deformation patterns of highly oriented nanotwins (*18*, *26*), we show that this unusual strengthening behavior is governed by bundles of concentrated dislocations in the grain interiors that help to accommodate large strain gradients and suppress strain localization. The gradient nanotwinned (GNT) structures provide a promising route to the design of new generations of high-performance metals.

Gradient nanotwinned structures

We used direct-current electrodeposition to prepare GNT Cu samples with a controllable patterning of homogeneous nanotwinned components. A typical GNT sample (GNT-1, Fig. 1A) has a patterning of homogeneous nanotwinned components we labeled ⒶⒷⒸⒹ, from bottom to top. We found no sharp interfaces between the homogeneous components from cross-sectional scanning electron microscopy (SEM) observations (Fig. 1B). Magnified SEM (Fig. 1, C and E) and transmission electron microscopy (TEM) (Fig. 1, D and F) observations of components Ⓐ and Ⓓ reveal that the individual components are composed of preferentially oriented nanometer-scale TBs embedded within the micrometer-scale columnar-shaped grains, with a mean aspect ratio of ~3. The selected-area electron diffraction (SAED) pattern and high-resolution TEM image (Fig. 1D, insets) show that the twin planes are coherent Σ3 boundaries. From component Ⓐ to component Ⓓ, the average twin thickness increases from 29 nm to 72 nm and the average grain size (defined as the size measured along the short axis) increases from 2.5 μm to 15.8 μm (Fig. 1G and fig. S1). To quantify the structural gradient of the GNT microstructure, we define a parameter, s, as the increment in hardness per unit thickness along the gradient direction. The cross-sectional hardness decreases gradually from 1.5 GPa in component Ⓐ to 0.8 GPa in component Ⓓ, resulting in a structural gradient of s = 1.75 GPa/mm in sample GNT-1 (Fig. 1H). By changing the stacking sequence of the homogeneous nanotwinned components while keeping the total sample thickness fixed at 400 μm, we designed three other GNT structures (GNT-2, GNT-3, and GNT-4) that possess various spatial distributions of the homogeneous components: ⒶⒷⒸⒹⒹ-ⒸⒷⒶ, 2×ⒶⒷⒸⒹⒹⒸⒷⒶ, and 4×ⒶⒷⒸⒹ-ⒹⒸⒷⒶ, respectively (fig. S2). Each homogeneous nanotwinned component has the same volume fraction of 25% and thickness of 100 μm in these GNT samples. The structural gradients of the GNT samples range from 1.75 to 11.6 GPa/mm, occupying the entire thickness of the sample (fig. S2D and tables S1 and S2) (*4*–*6*, *27*).

Strengthening and work-hardening ability

We compared engineering tensile stress-strain curves of the GNT samples to the tensile behaviors of the homogeneous nanotwinned components in free-standing conditions (Fig. 2A). The yield strength (σ_y), stress at 1% strain ($\sigma_{1\%}$), and ultimate tensile strength (σ_{uts}) of GNT-1, with the smallest s = 1.75 GPa/mm, are close to the average of the corresponding values of the four individual components indicated by the open symbols in Fig. 2B. As the structural gradient increases, both σ_y and σ_{uts} of the GNT structure gradually increase at the expense of a slight decrease in the uniform elongation (Table 1). In particular, GNT-4 exhibits a σ_y value of 481 ± 15 MPa that even exceeds the corresponding value of the strongest component Ⓐ, while its uniform elongation is 7%, larger than the corresponding values of components Ⓐ and Ⓑ. Meanwhile, the work-hardening rates, Θ, of the GNT samples are much higher than the average of the four homogeneous components, especially at strains less than 2% (Fig. 2C). We observed an increase with structural gradient for the work-hardening rate at ε = 1% (Fig. 2C, inset, and fig. S3). Surface morphologies indicate no surface cracking in GNT-4 before fracture

[1]Shengyang National Laboratory for Materials Science, Institute of Metal Research, Chinese Academy of Sciences, Shenyang 110016, China. [2]School of Materials Science and Engineering, University of Science and Technology of China, Shenyang 110016, China. [3]School of Engineering, Brown University, Providence, RI 02912, USA.
*These authors contributed equally to this work.
†Corresponding author. Email: huajian_gao@brown.edu (H.G.); llu@imr.ac.cn (L.L.)

failure, which further confirms that component Ⓐ sustains a large uniform elongation under a stress level much higher than its tensile strength measured in free-standing conditions. The above observations strongly suggest that a substantial strengthening effect can be achieved solely by increasing the structural gradient.

Post-mortem microstructures of GNT samples

Taking GNT-4 as an example, we characterized the post-mortem microstructures with SEM and TEM observations. Our observations (Fig. 3, A and E) show a class of unexpected parallel aligned dislocation bundles in the interior of the columnar grains at ε = 1% in both components Ⓐ and Ⓓ. Each dislocation bundle spans across multiple nanotwins and extends through almost the entire length of the grain perpendicular to TBs, marked by red arrows (Fig. 3, A and E), which coincides with the direction of the structural gradient in the GNT structure. Such dislocation patterns were observed in all nanotwinned components and have an average width that varies from 0.5 to 1.5 μm, as shown in the cross-sectional SEM images obtained by backscattered electrons (fig. S4).

We then adopted a two-beam diffraction technique (*26*) in TEM to determine the detailed configurations of the bundles of concentrated dislocations (BCDs), including the type, density, spatial arrangement, and Burgers vector of dislocations therein. We examined a typical BCD in component Ⓓ (Fig. 3A, white square) in TEM images (Fig. 3, B and C). We observed dislocation segments (identified by green arrows in Fig. 3B) with Burgers vectors of $\mathbf{b}_I$ = **DA**, **DB**, and **DC** (see the inset Thompson tetrahedron of Fig. 3A) inclined to the TBs by using a diffraction vector of $\mathbf{g}_M = \mathbf{g}_T$ = 111. We refer to these as mode I dislocations, following the definition in (*26*). Mode I dislocations are known to control the plastic deformation in highly oriented nanotwins when the loading direction is perpendicular to the TBs, leading to the classical Hall-Petch strengthening with reduced twin thickness (*18*). TEM observations confirmed that mode I dislocations are rarely observed in free-standing, homogeneous, highly oriented nanotwins when the loading direction is parallel to TBs (fig. S5).

Meanwhile, we observed a large amount of short dislocation segments (indicated by orange arrows in Fig. 3, C and D) located in the moiré fringes of the TBs with Burgers vectors of $\mathbf{b}_{II}$ =**AB**, **BC**, **CA** (Fig. 3A, inset) that are parallel to the twin planes by using a diffraction vector of $\mathbf{g}_M$ = 200. We call these mode II dislocations (*26*), which are often found to be prevalent in thin films (*24*), multilayered composites (*25*), and highly oriented nanotwinned structures (*18*, *26*).

In both components Ⓐ and Ⓓ, our observations show similar dislocation structures consisting of a majority of mode II dislocations (Fig. 3, C, D, G, and H) measured in and out of the BCDs (marked by the white square in Fig. 3, A and E), and much fewer mode I dislocations that span across multiple twin lamellae (Fig. 3, B and F). For instance, the BCDs we observed in components Ⓐ and Ⓓ contain mode II dislocations with a density of 2.1×10^{14} to 3.7×10^{14} m^{-2}, about

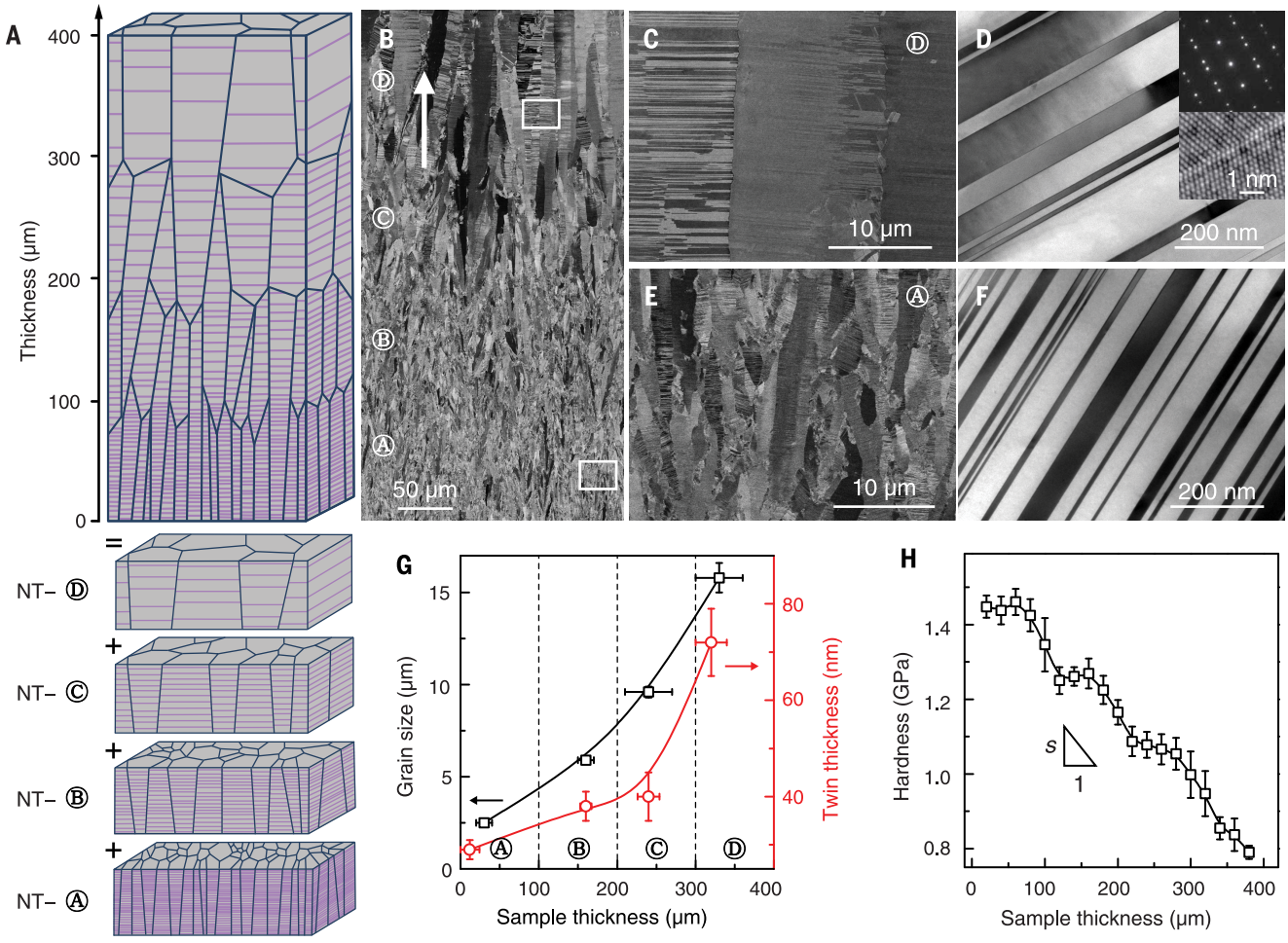

Fig. 1. Microstructure and structural gradient of a typical GNT specimen, GNT-1. (**A** and **B**) Schematics (A) and SEM observation (B) of GNT-1 composed of homogeneous nanotwinned components Ⓐ, Ⓑ, Ⓒ, and Ⓓ. In (B), gradient direction is indicated by the white arrow; white boxes outline the areas magnified in (C) to (F). (**C** to **F**) Magnified SEM and TEM images of components Ⓓ [(C) and (D)] and Ⓐ [(E) and (F)]. The insets in (D) show the SAED pattern and high-resolution TEM image of component Ⓓ. (**G**) Distribution of grain size and twin thickness along the sample thickness. (**H**) Distribution of hardness along the sample thickness. The vertical error bars in (G) and (H) represent standard deviations from statistical analyses with 500 (grain size), 1000 (twin thickness) and 5 to 10 (hardness) independent measurements, respectively. The horizontal error bars in (G) indicate the range of sample thickness of the measured samples.

an order of magnitude larger than that of mode I dislocations in the bundles (Table 2).

The observation of numerous BCDs containing both mode I and mode II dislocations in the grain interiors is distinct from the single activation of mode II dislocations that leads to strain localization near grain boundaries (GBs) in homogeneous nanotwinned samples at ε = 1% (fig. S5). In the latter case, only a negligible amount of mode I dislocations are detectable near the GBs, and mode II dislocations are randomly distributed in the columnar grains. Moreover, the average density of mode II dislocations in GNT-4 is measured to be about 1.7 × 10^{14} to 2.8 × 10^{14} m^{-2}, which is 4 to 8 times the densities observed in homogeneous nanotwinned samples (Table 2).

Atomistic simulations of extra strengthening in GNT Cu

To understand the underlying deformation mechanisms of the extra strengthening in GNT Cu, we performed large-scale fully three-dimensional atomistic simulations on samples that mimic the experimental setup. The largest simulation involves about 130 million atoms. A typical GNT simulation sample, GNT-ⒶⒷ, was created by combining two $[1\bar{1}1]$-textured homogeneous nanotwinned components (NT-Ⓐ and NT-Ⓑ) (Fig. 4A). We selected numbers of grains as n_A = 9 and n_B = 4 with average grain sizes of d_A = 30 nm and d_B = 50 nm, and twin thicknesses as λ_A = 0.83 nm and λ_B = 6.23 nm, respectively. By changing the thickness of the nongradient nanotwinned components, we tuned the structural gradient and created two different GNT samples with structural gradients of s = 6.2 MPa/nm (GNT-ⒶⒷ) and 12.4 MPa/nm (GNT-ⒶⒷⒶⒷ) (fig. S6, A and B). We measured the stress-strain curves of the GNT samples under uniaxial tensile loading along the x axis and compared them with the tensile responses of homogeneous samples NT-Ⓐ and NT-Ⓑ (Fig. 4B). Both gradient samples exhibit enhanced yield strength (defined as the average flow stress in the strain range of 6 to 15%) relative to their homogeneous counterparts. The strength increases with increasing structural gradient. We also performed simulations on GNT samples with statistically equivalent microstructures and observed the same extra strengthening effect (fig. S7). Thus, both our simulations and experiments demonstrate an unexpected ultrahigh strength in GNT Cu samples, which is higher than that of the strongest component of the structure.

Table 1. Tensile properties of GNT samples and free-standing homogeneous nanotwinned components. σ_y, yield strength; σ_{uts}, ultimate tensile strength; δ_u, uniform elongation.

Sample	σ_y (MPa)	σ_{uts} (MPa)	δ_u (%)
GNT-1	364 ± 12	397 ± 11	10 ± 2
GNT-2	434 ± 12	456 ± 15	9 ± 1
GNT-3	437 ± 19	471 ± 18	9 ± 1
GNT-4	481 ± 15	520 ± 12	7 ± 1
NT-Ⓐ	446 ± 10	470 ± 11	1 ± 0.5
NT-Ⓑ	394 ± 6	421 ± 5	6 ± 0.5
NT-Ⓒ	325 ± 4	350 ± 7	10 ± 0.5
NT-Ⓓ	223 ± 9	272 ± 4	22 ± 0.5

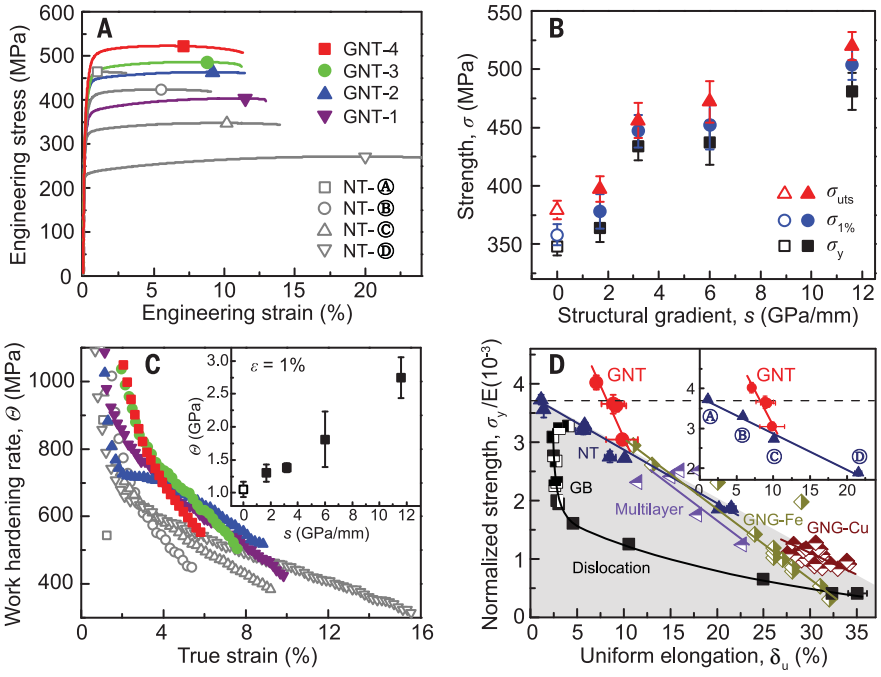

Fig. 2. Mechanical properties of GNT structures. (**A**) Tensile engineering stress-strain relations of GNT samples in comparison with those of homogeneous nanotwinned components. (**B**) Yield strength (σ_y), stress at ε = 1% ($\sigma_{1\%}$), and ultimate tensile strength (σ_{uts}) of GNT samples with various structural gradients. (**C**) Work-hardening rate and true strain relations of GNT samples compared with homogeneous components. The inset shows the variation of work-hardening rate measured at 1% strain with respect to structural gradient, s. Open symbols in (B) and (C) indicate average strength and work-hardening rate of the four homogeneous components. (**D**) Yield strength normalized by Young's modulus versus uniform elongation of GNT samples, in comparison with metals and alloys strengthened by dislocations (*43*), GBs (*44*, *45*), highly oriented nanotwins (*20*), and multilayered (*46*) and gradient nanograined (GNG) (*6*, *43*) structures. The inset shows the strengthening of GNT samples in comparison with homogeneous components. The error bars in (B) to (D) represent standard deviations from 6 to 12 independent tensile tests.

Formation mechanism of dislocation bundles in GNT Cu

The schematics (Fig. 4, C and D) illustrate typical deformation patterns of the GNT samples suggested by our experimental observations (Fig. 3). During deformation, a dislocation bundle forms in the interior of a nanotwinned columnar grain (colored pink) in the GNT structure (Fig. 4C). The bundle is composed of mode I dislocations intersecting with TBs and mode II dislocations gliding parallel to the TBs (Fig. 4D). We can show that the interactions between mode I and mode II dislocations in the dislocation bundles also lead to the formation of stair-rod dislocations (*22*).

We found from our simulations that upon yielding at ~4% strain, mode I dislocations (black triangles in Fig. 4, E and F, and fig. S8A) emit from the interface (*28*) toward nearby TBs. Meanwhile, mode II dislocations (black triangles in Fig. 4, G and H, and fig. S8A) are nucleated from lateral GBs. The simultaneous activation of mode I and II dislocations agrees with our experimental observations (Fig. 3). As the applied strain increased to 10%, a dislocation bundle was identified in the grain interior (fig. S8, B and C, and movie S1), where the dislocation density was measured as 2.2 × 10^{17} m^{-2}, almost an order of magnitude larger than that outside the dislocation bundle (fig. S8D). We found from our detailed analysis of the dislocation structures (Fig. 4I) that sessile stair-rod dislocations (in pink) account for about 15% of the total dislocation density. We attributed the formation of a typical stair-rod dislocation **δγ/BD** to the interaction between **γD** and **δB**, which are Shockley partial dislocations

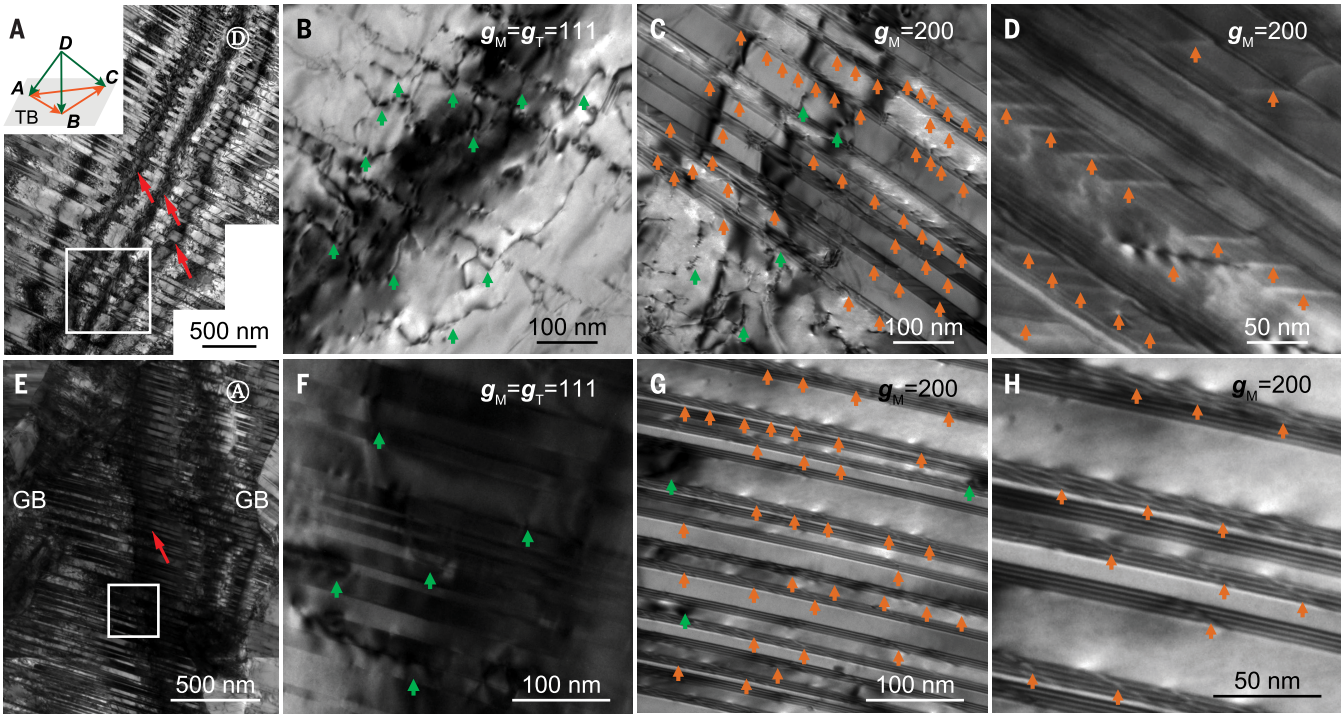

Fig. 3. Deformation microstructures of GNT-4 at 1% strain. (**A** and **E**) Bundles of concentrated dislocations (BCDs) are indicated by red arrows in components Ⓓ (A) and Ⓐ (E). (**B** and **C**) TEM images of the BCD region indicated by the white square in (A) identified by two-beam diffraction using vectors of $\mathbf{g}_M = \mathbf{g}_T$ = 111 (B) and $\mathbf{g}_M$ = 200 (C), respectively. (**D** and **H**) Magnified TEM images of the dislocations observed in (C) and (G), respectively. (**F** and **G**) TEM images of the BCD region indicated by the white square box in (E) identified by two-beam diffraction using vectors of $\mathbf{g}_M = \mathbf{g}_T$ = 111 (F) and $\mathbf{g}_M$ = 200 (G), respectively. Mode I dislocations are indicated by green arrows in (B), (C), (F), and (G); mode II dislocations are indicated by orange arrows in (C), (D), (G), and (H).

dissociated from mode I and mode II dislocations, respectively (Fig. 4J and fig. S8E). The movement of Shockley partial dislocations in the bundle region was thus substantially suppressed, contributing to additional strength enhancement (movie S2). For comparison, we observed a single slip mechanism governed by mode II dislocations and no formation of BCDs in the grain interior in homogeneous nanotwinned samples (fig. S9 and movie S3).

Table 2. Dislocation density measurement of bundles of concentrated dislocations (BCDs) and grain interiors for components Ⓐ and Ⓓ in GNT-4 and under free-standing homogeneous conditions at 1% strain.

Dislocation type	GNT-4, ρ (10^{13} m^{-2})				Homogeneous, ρ (10^{13} m^{-2})	
	Ⓐ		Ⓓ			
	BCD	Average	BCD	Average	Ⓐ	Ⓓ
Mode I	4.3	2.9	3.0	1.4	A few near GBs	
Mode II	36.7	28.3	20.6	17.4	7.2	2.3

Discussion

The storage of dislocations causes work hardening in crystals (*29*). For uniform plastic deformation, dislocations accumulate by trapping one another in a random way, giving rise to the storage of the so-called statistically stored dislocations (SSDs) (*9*). We found that as a result of the plastic strain gradients, the GNT components are not equally deformed during uniaxial tension (*30*). Component Ⓓ with lower yield strength plastically deforms before component Ⓒ. In a similar fashion, Ⓒ plastically deforms prior to Ⓑ. Component Ⓐ is the last to yield, leading to a gradient of plastic deformation in the GNT structure (fig. S10). In such circumstances, geometrically necessary dislocations (GNDs) (*9*–*13*) develop to accommodate the deformation gradients and allow compatible deformation among different components.

The concept of GNDs has been widely applied to explain size-dependent flow properties of crystals under nonuniform loading conditions including bending, torsion, indentation, and deformation at crack tips where stress and strain gradients are large (*10*, *11*, *31*, *32*). GNDs also explain the strengthening of polycrystalline metals (*9*), multilayer/multiphase metals (*33*–*35*), and gradient metals (*4*–*6*) due to inhomogeneous microstructures. However, the complex multiple slip systems in conventional materials make it challenging to distinguish GNDs from SSDs (*10*, *11*, *36*, *37*).

We took advantage of the simple deformation patterns of highly oriented coherent twins and found that the structural gradient in the GNT samples leads to the formation of a unique pattern of GNDs in the grain interiors (Fig. 3). These are in the form of BCDs composed of a majority of mobile mode II dislocations, which we never observed in free-standing nongradient nanotwinned components (fig. S5).

The local dislocation density we measured in the dislocation bundles is nearly 30% larger than the average dislocation density of the grain (Table 2), demonstrating the intense storage of GNDs in BCDs. We measured lattice rotation with a misorientation angle of ~5.2° for BCDs in component Ⓓ of GNT-4 (Fig. 3A) using an electron procession diffraction technique (*38*) in TEM, furthering demonstrating the concentration of GNDs in BCDs. Moreover, these concentrated GNDs may act as strong obstacles to slip and

accelerate the rate of statistical storage of dislocations in the material via long-range back stress (*35*, *39*, *40*), which increases substantially with structural gradient in the GNT samples (fig. S11). The GNT structures thus work-harden much faster than the nongradient nanotwinned samples (Fig. 2C). The average dislocation densities of GNT samples upon yielding are substantially elevated relative to those measured in the free-standing components (Table 2). For instance, at a small strain of 1%, the average dislocation density measured in GNT-4 is about 1.9 × 10^{14} to 3.1 × 10^{14} m^{-2}, which is an exceptionally high density of dislocations rarely reported in experiments (*41*). Interestingly, this value is also

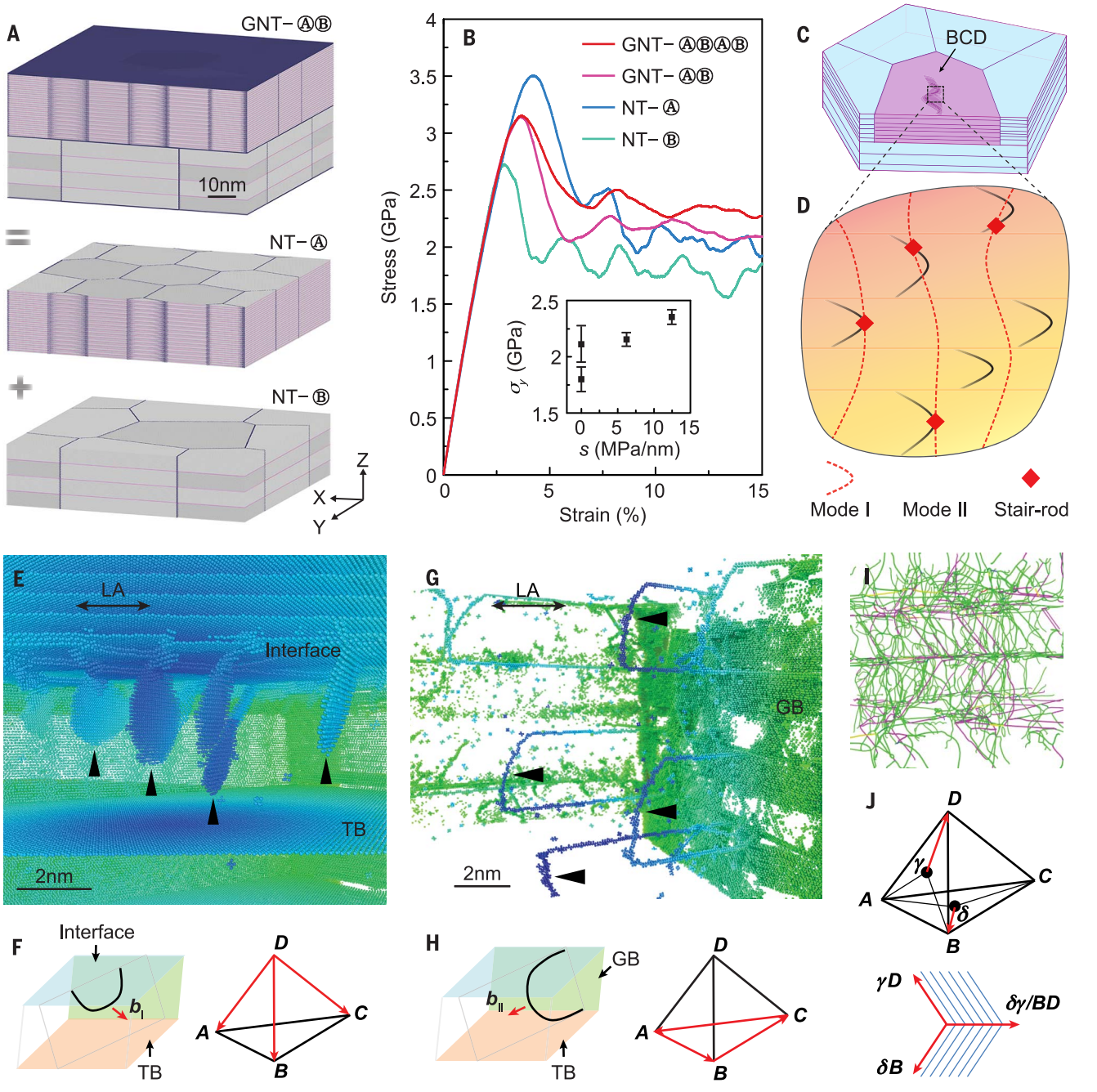

Fig. 4. GNT strengthening and associated deformation mechanisms by large-scale atomistic simulations. (**A**) Construction of a typical GNT structure, GNT-ⒶⒷ, through combinations of nanotwinned components NT-Ⓐ and NT-Ⓑ. (**B**) Stress-strain curves of GNT samples. The inset shows the relation between yield strength σ_y (the averaged flow stress from the strain range of 6 to 15%) and structural gradient *s*. Error bars represent the standard deviation from statistical analyses with 9000 sampling points. (**C**) Formation of a BCD in a nanotwinned grain (pink) in the GNT structure. (**D**) Zoom-in view of the BCD where interactions between mode I and mode II dislocations lead to stair-rod dislocations. (**E**) Emission of mode I dislocations (indicated by black triangles) from interface. (**F**) Schematic of mode I dislocations with Burgers vectors of **DA**, **DB**, and **DC**. (**G**) Emission of mode II dislocations (indicated by black triangles) from GBs. (**H**) Schematics of mode II dislocations with Burgers vectors of **AB**, **BC**, and **CA**. (**I**) High density of dislocations in the BCD composed of stair-rod dislocations (pink) and Shockley partial dislocations (green). (**J**) Schematics illustrating the formation of a stair-rod dislocation (**δγ/BD**).

two orders of magnitude higher than the density of GNDs (1.6×10^{12} m^{-2}) estimated from the plastic strain gradient along the thickness of the GNT structure, following Ashby's original work (*9*).

We can estimate the extra strengthening effect of the BCDs with Taylor's relation (*10*),

$$\Delta\sigma = M\alpha\mu b\left(\sqrt{\rho^{GNT}} - \sqrt{\rho^{NT}}\right) \quad (1)$$

where M = 3.17 is the Taylor factor of parallel loading with respect to TBs (*18*), μ = 42 GPa is the shear modulus of pure Cu, $b = 2.55 \times 10^{-10}$ m is the magnitude of the Burgers vector of dislocations, and α = 0.47 is the empirical constant for non-cell dislocations (*42*). We measured the total density of dislocations in components Ⓐ and Ⓓ of GNT-4 at 1% strain to be $\rho^{GNT} = 31.2 \times 10^{13}$ m^{-2} and 18.8×10^{13} m^{-2}, respectively; the corresponding values of the two components in their free-standing and homogeneous state are $\rho^{NT} = 7.2 \times 10^{13}$ m^{-2} and 2.3×10^{13} m^{-2}, respectively (Table 2). We support these values with our measurement that the back stresses of the GNT samples increase rapidly at low strains (fig. S11). The extra strength estimated from Eq. 1 is 146 MPa in component Ⓐ and 142 MPa in component Ⓓ. This agrees well with the extra yield strength of 134 MPa of GNT-4 (Fig. 2B).

The formation of BCDs also helps to delocalize plastic deformation as they are uniformly distributed inside the grains, unlike the strain concentration at GBs in nongradient components (fig. S5). Most important, our atomistic simulations show that most of the dislocations in BCDs are mobile Shockley partial dislocations (Fig. 4I), which are expected to accommodate large amounts of plastic deformation without a noticeable sacrifice in the ductility of the material (Fig. 2).

We compared the remarkable strength-ductility synergy of the GNT samples with various strengthening strategies reported in the literature (*6*, *43*–*46*) (Fig. 2D). We have normalized the strength by the Young's modulus of the materials. The gradient nanotwinned structure brings out an extra strengthening effect relative to homogeneous highly oriented nanotwins or multilayered materials strengthened by threading dislocations (*20*). In gradient nanograined structures, the density of GNDs is thought to be related to the plastic strain gradient (*30*). GNDs prefer to accumulate in the vicinity of GBs (*9*, *30*), inducing GB migration and grain coarsening or softening during plastic deformation (*4*). In contrast, by introducing a structural gradient in GNT structures, we obtained a high GND density in grain interiors (Table 2) and an exceptionally high strength exceeding that of the strongest component. When the structural gradient is sufficiently large, the strengthening effect of gradient nanotwins is superior to most existing gradient metals and alloys (*4*, *6*, *20*, *46*). The classical theory of strain gradient plasticity (*9*, *11*) only considers the plastic strain gradient due to incompatible plastic deformation in constituent components and may substantially underestimate the density of GNDs and the structural gradient strengthening in GNT structures.

Our observations point out the importance of designing gradient microstructures at multiple length scales in pursuit of high structural gradients for enhanced mechanical performance. The GNT strengthening strategy proposed in this work not only should help to advance the fundamental understanding of the processing-structure-property relationships of existing gradient-structured metals, but also suggests new challenges and opportunities for experimental, computational, and theoretical studies of next-generation metals and alloys.

Materials and methods

Materials

By means of direct-current electrodeposition technique, GNT Cu samples were fabricated by adjusting the electrolyte temperature in the range of 20° to 35°C. The current density was 30 mA/cm^2. The electrolyte was made with a $CuSO_4$ concentration of 90 g/liter. The pH value was ~1. The stirring speed was 1500 rpm and the additive concentration was 2 mg/liter. A commercial-purity Ti sheet was used as the cathode and a highly purified (99.995 wt %) Cu sheet was used as the anode. In the setup, the distance between the electrodes was kept as ~10 cm.

Various profiles of electrolyte temperature were used to synthesize GNT Cu samples (fig. S2B). The temperature was elevated stepwise (20°, 25°, 30°, 35°C) and preserved for 4 hours at each temperature to create GNT-1 with a spatial distribution of ⒶⒷⒸⒹ. The temperature rate, defined as temperature variation per hour, was 0.94°C/hour for GNT-1. Higher temperature rates of 1.88°C/hour, 3.75°C/hour, and 7.5°C/hour were used to fabricate GNT-2 (ⒶⒷⒸⒹⒹⒸⒷⒶ), GNT-3 (2×ⒶⒷⒸⒹⒹⒸⒷⒶ), and GNT-4 (4×ⒶⒷⒸⒹⒹⒸⒷⒶ), respectively (fig. S2, A and C). During the fabrication of the GNT samples, the total electrodeposition time was controlled to be 16 hours (i.e., 4 hours for each temperature) to ensure a sample thickness of about 400 μm and a volume fraction of 25% for each component.

For comparison, free-standing homogeneous nanotwinned Cu samples Ⓐ, Ⓑ, Ⓒ, and Ⓓ were constructed by electrodeposition at 20°, 25°, 30°, and 35°C, respectively. A total deposition time of 16 hours resulted in a sample thickness of about 400 μm.

Uniaxial tensile tests

For tensile tests, dog bone–shaped flat specimens with a gauge length of 5 mm and width of 2 mm were cut from the as-deposited GNT and nanotwinned Cu sheets using an electric spark machine. Before tensile tests, all tensile specimens were mechanically and electrochemically polished to minimize surface roughness. Uniaxial quasi-static tensile tests were carried out in an Instron 5848 micro tester with a 2-kN load cell at a strain rate of 5×10^{-3} s^{-1} at ambient temperature. During tensile tests, a contactless MTS LX300 laser extensometer was used to calibrate and measure the strain in the gauge. To confirm reproducibility, we repeated tensile tests 6 to 12 times for each structure, from which average values and standard errors were calculated for yield strength (at 0.2% offset strain), stress at 1% strain, ultimate tensile strength, and uniform elongation.

Micro-hardness measurements

Cross-sectional micro-hardness measurements were performed along the thickness of the GNT samples on a Qness Q10A+ micro-hardness tester with a load of 50 g and a loading time of 10 s. For each depth, 5 to 10 independent measurements were conducted.

Microstructure observations

Cross-sectional microstructures of GNT samples were characterized in a FEI NovaSEM 430 field emission gun SEM using backscattering electron imaging with a high-contrast (vCD) detector. The average grain size obtained from the SEM images was measured over 500 grains for each depth of the GNT samples. Samples were mechanically polished and electrochemically polished in a solution of phosphoric acid (25%), alcohol (25%), and deionized water (50%) at ambient temperature before SEM observations.

Cross-sectional microstructures of as-deposited and deformed GNT samples were also examined using a FEI Tecnai G2 F20 TEM operated at 200 kV. The average twin thickness was obtained from TEM images with edge-on TBs and was measured over 1000 twin lamellae for each depth of the GNT samples. A two-beam diffraction technique (*26*) was used to identify the type of dislocations (*18*, *26*) in the deformed GNT and free-standing nanotwinned samples. The TEM foils of the deformed samples were sliced from the gauge section along the direction parallel to the tensile axis. Each TEM foil was attached to a Cu ring 3 mm in diameter and thinned by twin-jet electrochemical polishing in a solution of phosphoric acid (25%), alcohol (25%), and deionized water (50%) at about −10°C.

Computational GNT Cu samples

Three GNT Cu samples were constructed for atomistic simulations (fig. S6). We started by building two homogeneous columnar-grained nanotwinned components (Fig. 4A), NT-Ⓐ and NT-Ⓑ, each having a $[1\bar{1}\bar{1}]$ our-of-plane texture and zero structural gradient (i.e., s = 0). By varying the thickness of the individual components and combining them in different stacking sequences (e.g., ⒶⒷ or ⒶⒷⒶⒷ), GNT samples with various structural gradients can be generated.

The homogeneous components NT-Ⓐ and NT-Ⓑ used to generate GNT-ⒶⒷ (fig. S6A) and GNT-ⒶⒷⒶⒷ (fig. S6B) have grain numbers of n_A = 9 and n_B = 4, average grain sizes of d_A = 30 nm and d_B = 50 nm, and twin thicknesses of λ_A = 0.83 nm and λ_B = 6.3 nm, respectively. The thicknesses of NT-Ⓐ and NT-Ⓑ are 25 nm in GNT-ⒶⒷ and 12.5 nm in GNT-ⒶⒷⒶⒷ. The volume fractions of NT-Ⓐ and NT-Ⓑ are equal in both GNT-ⒶⒷ and GNT-ⒶⒷⒶⒷ. Both GNT-ⒶⒷ and GNT-ⒶⒷⒶⒷ contain ~42,000,000 atoms and have dimensions of ~$100 \times 100 \times 50$ nm^3.

The homogeneous components NT-Ⓐ and NT-Ⓑ used to generate GNT-ⒶⒷ-2 (fig. S6C) have thicknesses of h_A = 6.3 nm and h_B = 33.2 nm, grain numbers of n_A = 400 and n_B = 4, average grain sizes of d_A = 10 nm and d_B = 100 nm, and twin thicknesses of λ_A = 0.63 nm and λ_B = 8.3 nm, respectively. The entire sample contains ~130,000,000 atoms and has dimensions of ~200 × 200 × 40 nm^3. The much larger "in-plane" size of GNT-ⒶⒷ-2 allows us to capture the formation process of a BCD in the interior of the nanotwinned grains. The large number of triple junctions at the interface between components NT-Ⓐ and NT-Ⓑ are potential dislocation sources during deformation (*28*).

The same relaxation, tension, and visualization methods were adopted for the simulated samples. Specifically, the system was initially equilibrated for 500 ps at 300 K, followed by uniaxial tensile loading along the x axis to a total strain of 15% at a constant strain rate of 2×10^8 s^{-1}. Throughout the simulation, periodic boundary conditions were applied in all three directions. Constant temperature and zero pressure in the nonstretching directions (i.e., y and z axes) were controlled by Nose-Hoover thermostatting and barostatting (*47*, *48*). The embedded atom method potential was used to compute the interatomic forces (*49*), and the integration time step was fixed at 1 fs. The common neighbor analysis (CNA) method (*50*) was used to identify defects that emerge during plastic deformation. A position-based coloring scheme (*19*) was used to visualize defects in which colors are assigned according to the spatial coordinates of atoms.

Calculation of dislocation density of GNDs from plastic strain gradient

Following Ashby's original work (*9*), the density of GNDs, ρ^{GNT}, was calculated by

$$\rho^{GNT} = \frac{\eta}{b} \quad (2)$$

where b = 2.55 × 10^{-10} m is the magnitude of the Burgers vector of dislocations, and η is the average plastic strain gradient in GNT calculated through

$$\eta = \frac{\varepsilon_p^D - \varepsilon_p^A}{t_{AD}} \quad (3)$$

where ε_p^A and ε_p^D are the plastic strains of components Ⓐ and Ⓓ, respectively. The spacing between components Ⓐ and Ⓓ, t_{AD}, increases with the structural gradient s. The difference in the plastic strain ($\varepsilon_p^D - \varepsilon_p^A$), originating from the different yield strengths of components Ⓐ and Ⓓ, reaches a maximum value of ~0.2% and remains constant after component Ⓐ yields. The density of GNDs was calculated to be 1.6 × 10^{12} m^{-2} in GNT-4, assuming that it is proportional to the plastic strain gradient.

Back stress measurement

A gauging system including a Navitar Zoom 6000 optic lens with a magnification of 2 and a high-resolution charge-coupled device (CCD) camera (2088 × 1024 pixels) (*51*) was applied to measure the strain during loading-unloading tensile tests. The back stress was obtained from unloading curves with an offset plastic strain of 0.01% and a slope equal to the Young's modulus E according to the Dickson method (*38*, *51*, *52*).

Misorientation mapping of BCDs

Misorientation of BCDs in GNT samples was measured by means of an electron procession diffraction technique in TEM using NanoMEGAS (Brussels, Belgium) hardware and ASTAR system. The BCD region was scanned by a nanoscale beam with a step of 3.6 nm, and the electron diffraction pattern at each scanned point was collected using a fast CCD camera, providing the misorientation mapping of BCDs. Details about the electron procession diffraction technique can be found in (*38*, *53*).

REFERENCES AND NOTES

1. K. Lu, L. Lu, S. Suresh, Strengthening materials by engineering coherent internal boundaries at the nanoscale. *Science* **324**, 349–352 (2009). doi: 10.1126/science.1159610; pmid: 19372422
2. Z. Liu, M. A. Meyers, Z. Zhang, R. O. Ritchie, Functional gradients and heterogeneities in biological materials: Design principles, functions, and bioinspired applications. *Prog. Mater. Sci.* **88**, 467–498 (2017). doi: 10.1016/j.pmatsci.2017.04.013
3. S. Suresh, Graded materials for resistance to contact deformation and damage. *Science* **292**, 2447–2451 (2001). doi: 10.1126/science.1059716; pmid: 11431558
4. T. H. Fang, W. L. Li, N. R. Tao, K. Lu, Revealing extraordinary intrinsic tensile plasticity in gradient nano-grained copper. *Science* **331**, 1587–1590 (2011). doi: 10.1126/science.1200177; pmid: 21330487
5. Y. Wei *et al*., Evading the strength-ductility trade-off dilemma in steel through gradient hierarchical nanotwins. *Nat. Commun.* **5**, 3580 (2014). doi: 10.1038/ncomms4580; pmid: 24686581
6. X. Wu, P. Jiang, L. Chen, F. Yuan, Y. T. Zhu, Extraordinary strain hardening by gradient structure. *Proc. Natl. Acad. Sci. U.S.A.* **111**, 7197–7201 (2014). doi: 10.1073/pnas.1324069111; pmid: 24799688
7. S. Zhao *et al*., Generating gradient germanium nanostructures by shock-induced amorphization and crystallization. *Proc. Natl. Acad. Sci. U.S.A.* **114**, 9791–9796 (2017). doi: 10.1073/pnas.1708853114; pmid: 28847926
8. R. Thevamaran *et al*., Dynamic creation and evolution of gradient nanostructure in single-crystal metallic microcubes. *Science* **354**, 312–316 (2016). doi: 10.1126/science.aag1768; pmid: 27846562
9. M. F. Ashby, The deformation of plastically non-homogeneous materials. *Philos. Mag.* **21**, 399–424 (1970). doi: 10.1080/14786437008238426
10. N. A. Fleck, G. M. Muller, M. F. Ashby, J. W. Hutchinson, Strain gradient plasticity: Theory and experiment. *Acta Metall. Mater.* **42**, 475–487 (1994). doi: 10.1016/0956-7151(94)90502-9
11. H. Gao, Y. Huang, W. D. Nix, J. W. Hutchinson, Mechanism-based strain gradient plasticity I. Theory. *J. Mech. Phys. Solids* **47**, 1239–1263 (1999). doi: 10.1016/S0022-5096(98)00103-3
12. M. E. Gurtin, L. Anand, A theory of strain-gradient plasticity for isotropic, plastically irrotational materials. Part I: Small deformations. *J. Mech. Phys. Solids* **53**, 1624–1649 (2005). doi: 10.1016/j.jmps.2004.12.008
13. N. A. Fleck, M. F. Ashby, J. W. Hutchinson, The role of geometrically necessary dislocations in giving material strengthening. *Scr. Mater.* **48**, 179–183 (2003). doi: 10.1016/S1359-6462(02)00338-X
14. T. Roland, D. Retraint, K. Lu, J. Lu, Fatigue life improvement through surface nanostructuring of stainless steel by means of surface mechanical attrition treatment. *Scr. Mater.* **54**, 1949–1954 (2006). doi: 10.1016/j.scriptamat.2006.01.049
15. J. Li, S. Chen, X. Wu, A. Soh, J. Lu, The main factor influencing the tensile properties of surface nano-crystallized graded materials. *Mater. Sci. Eng. A* **527**, 7040–7044 (2010). doi: 10.1016/j.msea.2010.07.064
16. X. Wu *et al*., Synergetic strengthening by gradient structure. *Mater. Res. Lett.* **2**, 185–191 (2014). doi: 10.1080/21663831.2014.935821
17. L. Lu, Y. Shen, X. Chen, L. Qian, K. Lu, Ultrahigh strength and high electrical conductivity in copper. *Science* **304**, 422–426 (2004). doi: 10.1126/science.1092905; pmid: 15031435
18. Z. You *et al*., Plastic anisotropy and associated deformation mechanisms in nanotwinned metals. *Acta Mater.* **61**, 217–227 (2013). doi: 10.1016/j.actamat.2012.09.052
19. Q. Pan, H. Zhou, Q. Lu, H. Gao, L. Lu, History-independent cyclic response of nanotwinned metals. *Nature* **551**, 214–217 (2017). pmid: 29088707
20. Z. S. You, L. Lu, K. Lu, Tensile behavior of columnar grained Cu with preferentially oriented nanoscale twins. *Acta Mater.* **59**, 6927–6937 (2011). doi: 10.1016/j.actamat.2011.07.044
21. I. J. Beyerlein, X. Zhang, A. Misra, Growth twins and deformation twins in metals. *Annu. Rev. Mater. Res.* **44**, 329–363 (2014). doi: 10.1146/annurev-matsci-070813-113304
22. Z. X. Wu, Y. W. Zhang, D. J. Srolovitz, Dislocation–twin interaction mechanisms for ultrahigh strength and ductility in nanotwinned metals. *Acta Mater.* **57**, 4508–4518 (2009). doi: 10.1016/j.actamat.2009.06.015
23. J. Wang *et al*., Detwinning mechanisms for growth twins in face-centered cubic metals. *Acta Mater.* **58**, 2262–2270 (2010). doi: 10.1016/j.actamat.2009.12.013
24. W. D. Nix, Yielding and strain hardening of thin metal films on substrates. *Scr. Mater.* **39**, 545–554 (1998). doi: 10.1016/S1359-6462(98)00195-X
25. A. Misra, J. P. Hirth, R. G. Hoagland, Length-scale-dependent deformation mechanisms in incoherent metallic multilayered composites. *Acta Mater.* **53**, 4817–4824 (2005). doi: 10.1016/j.actamat.2005.06.025
26. Q. Lu, Z. You, X. Huang, N. Hansen, L. Lu, Dependence of dislocation structure on orientation and slip systems in highly oriented nanotwinned Cu. *Acta Mater.* **127**, 85–97 (2017). doi: 10.1016/j.actamat.2017.01.016
27. H. T. Wang, N. R. Tao, K. Lu, Architectured surface layer with a gradient nanotwinned structure in a Fe–Mn austenitic steel. *Scr. Mater.* **68**, 22–27 (2013). doi: 10.1016/j.scriptamat.2012.05.041
28. R. J. Asaro, S. Suresh, Mechanistic models for the activation volume and rate sensitivity in metals with nanocrystalline grains and nano-scale twins. *Acta Mater.* **53**, 3369–3382 (2005). doi: 10.1016/j.actamat.2005.03.047
29. U. F. Kocks, H. Mecking, Physics and phenomenology of strain hardening: The FCC case. *Prog. Mater. Sci.* **48**, 171–273 (2003). doi: 10.1016/S0079-6425(02)00003-8
30. Z. Zeng *et al*., Gradient plasticity in gradient nano-grained metals. *Extreme Mech. Lett.* **8**, 213–219 (2016). doi: 10.1016/j.eml.2015.12.005
31. J. G. Swadener, E. P. George, G. M. Pharr, The correlation of the indentation size effect measured with indenters of various shapes. *J. Mech. Phys. Solids* **50**, 681–694 (2002). doi: 10.1016/S0022-5096(01)00103-X
32. S. S. Chakravarthy, W. A. Curtin, Stress-gradient plasticity. *Proc. Natl. Acad. Sci. U.S.A.* **108**, 15716–15720 (2011). doi: 10.1073/pnas.1107035108; pmid: 21911403
33. M. Kouzeli, A. Mortensen, Size dependent strengthening in particle reinforced aluminium. *Acta Mater.* **50**, 39–51 (2002). doi: 10.1016/S1359-6454(01)00327-5
34. X. Ma *et al*., Mechanical properties of copper/bronze laminates: Role of interfaces. *Acta Mater.* **116**, 43–52 (2016). doi: 10.1016/j.actamat.2016.06.023
35. X. Wu *et al*., Heterogeneous lamella structure unites ultrafine-grain strength with coarse-grain ductility. *Proc. Natl. Acad. Sci. U.S.A.* **112**, 14501–14505 (2015). doi: 10.1073/pnas.1517193112; pmid: 26554017
36. G. A. Malygin, Dislocation mechanism of dynamic polygonization of a crystal caused by its bending. *Phys. Solid State* **44**, 1249–1253 (2002). doi: 10.1134/1.1494626
37. D. A. Hughes, N. Hansen, D. J. Bammann, Geometrically necessary boundaries, incidental dislocation boundaries and geometrically necessary dislocations. *Scr. Mater.* **48**, 147–153 (2003). doi: 10.1016/S1359-6462(02)00358-5
38. D. Viladot *et al*., Orientation and phase mapping in the transmission electron microscope using precession-assisted diffraction spot recognition: State-of-the-art results. *J. Microsc.* **252**, 23–34 (2013). doi: 10.1111/jmi.12065; pmid: 23889078
39. X. Feaugas, On the origin of the tensile flow stress in the stainless steel AISI 316L at 300 K: Back stress and effective stress. *Acta Mater.* **47**, 3617–3632 (1999). doi: 10.1016/S1359-6454(99)00222-0
40. H. Mughrabi, Deformation-induced long-range internal stresses and lattice plane misorientations and the role of geometrically necessary dislocations. *Philos. Mag.* **86**, 4037–4054 (2006). doi: 10.1080/14786430500509054

41. T. Ungár, E. Schafler, P. Hanák, S. Bernstorff, M. Zehetbauer, Vacancy production during plastic deformation in copper determined by in situ X-ray diffraction. *Mater. Sci. Eng. A* **462**, 398–401 (2007). doi: 10.1016/j.msea.2006.03.156
42. T. Ungár, A. D. Stoica, G. Tichy, X. L. Wang, Orientation-dependent evolution of the dislocation density in grain populations with different crystallographic orientations relative to the tensile axis in a polycrystalline aggregate of stainless steel. *Acta Mater.* **66**, 251–261 (2014). doi: 10.1016/j.actamat.2013.11.012
43. K. Lu, Gradient nanostructured materials. *Acta Metall. Sin.* **51**, 1–10 (2015). doi: 10.11900/0412.1961.2014.00395
44. P. Zhang, S. X. Li, Z. F. Zhang, General relationship between strength and hardness. *Mater. Sci. Eng. A* **529**, 62–73 (2011). doi: 10.1016/j.msea.2011.08.061
45. K. Edalati, T. Fujioka, Z. Horita, Microstructure and mechanical properties of pure Cu processed by high-pressure torsion. *Mater. Sci. Eng. A* **497**, 168–173 (2008). doi: 10.1016/j.msea.2008.06.039
46. X. L. Ma *et al*., Strain hardening and ductility in a coarse-grain/nanostructure laminate material. *Scr. Mater.* **103**, 57–60 (2015). doi: 10.1016/j.scriptamat.2015.03.006
47. W. G. Hoover, Constant-pressure equations of motion. *Phys. Rev. A* **34**, 2499–2500 (1986). doi: 10.1103/PhysRevA.34.2499; pmid: 9897546
48. S. Nosé, A unified formulation of the constant temperature molecular dynamics methods. *J. Chem. Phys.* **81**, 511–519 (1984). doi: 10.1063/1.447334
49. Y. Mishin, M. J. Mehl, D. A. Papaconstantopoulos, A. F. Voter, J. D. Kress, Structural stability and lattice defects in copper: *Ab initio*, tight-binding, and embedded-atom calculations. *Phys. Rev. B* **63**, 224106 (2001). doi: 10.1103/PhysRevB.63.224106
50. D. Faken, H. Jonsson, Systematic analysis of local atomic structure combined with 3D computer graphics. *Comput. Mater. Sci.* **2**, 279–286 (1994). doi: 10.1016/0927-0256(94)90109-0
51. H. Wang, Z. You, L. Lu, Kinematic and isotropic strain hardening in copper with highly aligned nanoscale twins. *Mater. Res. Lett.* **6**, 333–338 (2018). doi: 10.1080/21663831.2018.1455752
52. J. I. Dickson, J. Boutin, L. Handfield, A comparison of two simple methods for measuring cyclical internal and effective stresses. *Mater. Sci. Eng.* **64**, L7–L11 (1984). doi: 10.1016/0025-5416(84)90083-1
53. W. Xu, X. Liu, K. Lu, Strain-induced microstructure refinement in pure Al below 100 nm in size. *Acta Mater.* **152**, 138–147 (2018). doi: 10.1016/j.actamat.2018.04.014

ACKNOWLEDGMENTS

We thank N. R. Tao, T. Zhu, N. Hansen, and X. X. Huang for inspirational discussions, and S. Jin for samples preparation.

Funding: Supported by NSFC grants 51471172 and U1608257, the Key Research Program of Frontier Science, CAS and the National Basic Research Program of China (973 Program, 2012CB932202) (L.L.); NSFC International collaboration grant 51420105001 (L.L. and H.G.); and NSF grant DMR-1709318 and XSEDE grant MS090046 (H.Z. and H.G.). **Author contributions:** L.L. and H.G. conceived and led the project; Z.C., Q.L., and L.L. performed the experiments; H.Z. performed the simulations; and all authors wrote and approved the submitted manuscript. **Competing interests:** None declared. **Data and materials availability:** The data generated in this study are included in the manuscript and its supplementary materials. Atomistic simulations were performed using LAMMPS, which is freely available at http://lammps.sandia.gov/.

SUPPLEMENTARY MATERIALS

www.sciencemag.org/content/362/6414/eaau1925/suppl/DC1
Figs. S1 to S11
Tables S1 and S2
Movies S1 to S3

16 May 2018; accepted 7 September 2018
10.1126/science.aau1925

Extra strengthening and work hardening in gradient nanotwinned metals

Zhao Cheng, Haofei Zhou, Qiuhong Lu, Huajian Gao and Lei Lu

Science **362** (6414), eaau1925.
DOI: 10.1126/science.aau1925

Stronger copper through twin power

Materials with structural gradients often have unique combinations of properties. Gradient-structured materials are found in nature and can be engineered. Cheng *et al.* made a structural gradient by introducing gradients of crystallographic twins into copper. This strategy creates bundles of dislocations in the crystal interiors, which makes the metal stronger than any of the individual components. This method offers promise for developing high-performance metals.

Science, this issue p. eaau1925